



Article

Investigation of Friction Hydro-Pillar Processing as a Repair Technique for Offshore Mooring Chain Links

Rafael Eugenio dos Santos ¹, Mariane Chludzinski ^{2,*}, Rafael Menezes Nunes ³, Ricardo Reppold Marinho ⁴, Marcelo Torres Piza Paes ⁴ and Afonso Reguly ¹

- ¹ Physical Metallurgy Laboratory (LAMEF), Universidade Federal do Rio Grande do Sul (UFRGS), Av. Bento Gonçalves, 9500, Porto Alegre 91501-970, Brazil; rafaeleugeniiodossantos@gmail.com (R.E.d.S.); reguly@demet.ufrgs.br (A.R.)
- ² LORTEK, Basque Research and Technology Alliance (BRTA), Arranomendia kalea 4A, 20240 Ordizia, Spain
- ³ Metalforming Laboratory (LdTM), Universidade Federal do Rio Grande do Sul (UFRGS), Av. Bento Gonçalves, 9500, Porto Alegre 91501-970, Brazil; rafael.nunes@ufrgs.br
- ⁴ Research and Development Center, Petrobras, Rio de Janeiro 21941-915, Brazil; reppold@petrobras.com.br (R.R.M.); mtpp@petrobras.com.br (M.T.P.P.)
- * Correspondence: mchludzinski@lortek.es

Abstract: Repairing links of offshore mooring chains has presented a significant industry challenge, primarily arising from modifications in material properties, encompassing alterations in microstructure, hardness, and residual stress. In this context, the present work investigates the method of friction hydro-pillar processing (FHPP) applied to R4 grade mooring chain steel. Joints in as-repaired and post-weld heat treatment (PWHT) conditions were subjected to residual stress (RS) tests using the neutron diffraction technique, microhardness mapping, and microstructural evaluations. The process generated peaks of tensile and compressive stresses in different directions and hardness below that of the parent material in the softening zone. The friction zone promoted high hardness levels in the thermo-mechanically affected zone (TMAZ) with a maximum of 19% of the ultimate tensile strength of the parent material. As expected, the PWHT restored the RS and reduced the hardness; however, 4 h PWHT allowed the elimination of a hardness higher than that of the base material.

Keywords: friction hydro-pillar processing; mooring steel grade R4; PWHT; residual stress; neutron diffraction



Citation: dos Santos, R.E.; Chludzinski, M.; Nunes, R.M.; Marinho, R.R.; Paes, M.T.P.; Reguly, A. Investigation of Friction Hydro-Pillar Processing as a Repair Technique for Offshore Mooring Chain Links. *J. Manuf. Mater. Process.* **2023**, *7*, 200. <https://doi.org/10.3390/jmmp7060200>

Academic Editor: Yu-Ming Zhang

Received: 14 September 2023

Revised: 30 October 2023

Accepted: 4 November 2023

Published: 9 November 2023



Copyright: © 2023 by the authors. Licensee MDPI, Basel, Switzerland. This article is an open access article distributed under the terms and conditions of the Creative Commons Attribution (CC BY) license (<https://creativecommons.org/licenses/by/4.0/>).

1. Introduction

Offshore fields have been essential energy source areas of exploration. Oil and gas and wind farm companies have reached these fields using fixed and floating structures. In the shallow waters, foundations are built rigidly on the seabed; however, ships, windmills, and floating platforms in deep and ultra-deep waters are anchored. Mooring systems between the platform and the anchor are composed of wires and ropes in the middle, high-strength steel chains at both ends, and accessories. The mooring systems are designed to limit the platform movement and provide protection against the hostile environment of corrosion, thermal gradients, high water pressures, and fatigue stresses from winds, marine currents, and waves. Furthermore, the chain links require additional wear resistance due to the friction on anchors, seabed, and machinery deck, as seen in mooring windlasses, fairleads, and chain stopper platforms [1]. With their service life prediction of about 30 years under these conditions, regulatory standard guidelines derived from the International Association of Classification Societies section W22 (IACS) [2] have established the minimal material properties, including manufacturing processes, to guarantee the structural integrity of links. From an economic perspective, the requirements increase the manufacturing costs, especially due to non-compliant components being discarded. In accordance with integrity recommendation, bars supplied with injurious surface imperfections, such as seams, laps

and rolled-in mill scale, are not allowed if the imperfection depth is greater than 1% of the bar diameter. In addition, after carrying out proof load testing on the mooring chains, superficial imperfections (cracks, cuts, or defects) in the flash welding zone can be ground up to 5% of the diameter in depth. However, links with higher levels of defects than acceptable shall be replaced, and only up to three links (splice links) can be changed before the rejection of the entire chain. Furthermore, repairing links by welding is not permitted in such cases due to the modification of the material properties [2].

In this sense, less conventional weld repair technologies have been investigated to ensure high quality and reduce production costs. Friction welding methods, for example, have shown advantages compared to conventional arc welding processes [3]. Since these techniques reach temperatures below melting point, the components undergo thermal-mechanical effects, and the welding issues related to the solidification stage are avoided [4]. As these are automatized processes, repeatability and reproducibility are guaranteed; in addition, the low emission of gases and radiation characterizes them as eco-friendly processes [3,5]. In addition, the low temperature involved allows the welding of similar and dissimilar materials, avoiding melting defects [3,6–8]. As presented by Vyas et al. [9], the solid-state process generated reliable Al-steel joints. Similarly, Joshi et al. [10] employed friction welding to join copper with stainless steel, avoiding induced thermal stress mismatches, complex surface tension, and multiple-element solidification effects.

These methods use temperature generated from the friction of the relative movement of two faying surfaces. As observed in rotary friction welding, two cylindrical surfaces (bars or pipes) undergo relative rotary motion while experiencing axial force in the first phase and forging in the second phase. This method has been widely used for decades due to its simple geometry and movement [11]. There are two variations of energy input: direct drive, where the velocity of one workpiece is controlled by an electric engine, and inertia drive, where energy from a flywheel is transferred to a workpiece. In both cases, another workpiece is prevented from rotating [12]. As the inertia-drive friction welding delivers a decreased movement, the thermo-mechanical cycle involves distinct stages. The process begins with an instantaneous discharge of kinetic energy that generates heat on the faying surfaces at high strain rates. As the temperature increases and the rotation decreases, the joint undergoes a plastic flow stage until frictional shear stresses become independent of normal pressure. Subsequently, when the flywheel reaches a low rotatory velocity, this behavior is replaced with a sticking condition [13]. The controlled welding parameters in inertia-drive friction include the moment of inertia, rotational speed, specific load, and specific energy [14]. In contrast, direct-drive friction relies on controlled spin velocity that provides several welding parameters such as friction time, forging time, friction pressure, forge pressure, and rotational speed [15].

Several other methods have been developed over the years, including friction stud welding, linear and orbital friction welding, friction taper stitch welding, friction stir welding, friction surface welding, and friction girth welding. Nevertheless, friction hydro-pillar processing (FHPP) is an effective repair method that replaces defective zones with sound materials with the same or even superior chemical composition and mechanical properties. The Welding Institute developed this process with a patent granted in 1995 [16]. This process consists of filling a blind hole previously drilled in the base material (BM) with a consumable stud. The high rotation speed applied under an axial force on the faying surfaces generates enough heat to soften the parent materials (stud and BM). Therefore, the stud is plastically deformed in a series of shear planes flowing radially in an upward direction [4]. During the process, the axial force applied to the spinning stud is divided into both vertical and horizontal directions due to the enclosure environment created in the blind hole. The flow of the material in a viscous condition undergoes a hydrostatic force to consolidate the joint against the sidewalls [12,16,17]. The process ends when the pre-set displacement (burn-off) is achieved, quickly stopping the rotation while an additional forging force is applied (Figure 1).

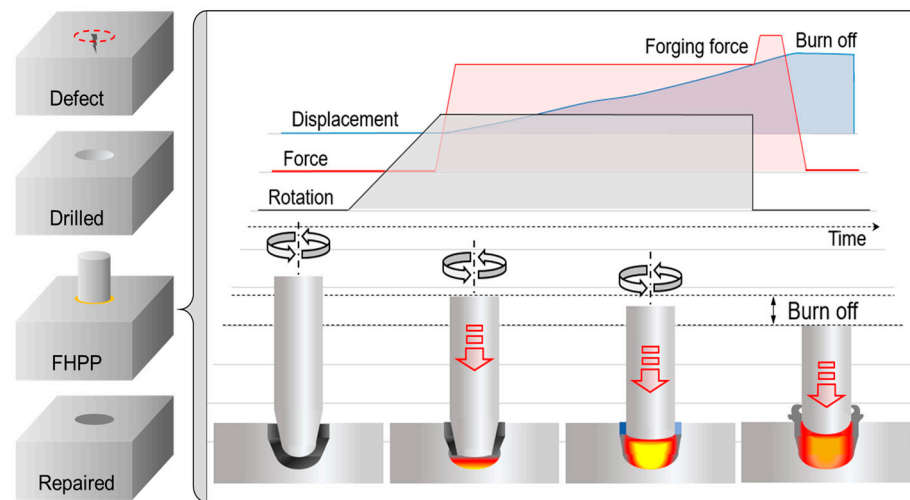


Figure 1. Schematic progress of FHPP.

As a friction solid-state process, it involves high levels of plastic deformation, although the temperature reached is considered low (below the melting point) compared to fusion processes. Nevertheless, residual stresses (RSs) are associated with inhomogeneous thermal distribution, plastic deformation, and phase transformations [3,18]. This aspect is extremely relevant since the RS has various effects on the performance of materials, such as fracture toughness, fatigue life, and stress corrosion cracking. For instance, the tensile stress profile reduces fatigue life [19] and increases hydrogen absorption [20]. Besides the welding characteristics, other intrinsic and extrinsic factors substantially impact the joint RS, such as the material manufacturing process, welding parameters, thermal treatments, microstructure formation, and hole/stud geometries. In this sense, there are some destructive and non-destructive techniques for evaluating RS. The non-destructive methods, including X-ray and neutron diffraction techniques, can provide reliable details about the stress fields, especially in the weld seams. The neutron diffraction technique has shown advantages, such as high sensitivity and the ability to analyze thick materials due to its high penetration capacity (up to 200 mm in Al or 25 mm in Fe) [21].

Some investigations have used the neutron diffraction technique to analyze the RS generated in friction repair processes. The study carried out by Paes [22] using structural steel S3555 J2G3 indicated tensile RS measurements in the stud region, changing to compressive stresses towards the BM. In addition, increasing the axial force (from 50 to 400 kN) reduced the tensile RS peak (65% tangential and 57% radial), generating a beneficial effect due to the faster process time involved and, consequently, less stud material processed. Hattingh et al. [23] studied friction taper stud-welded 10CrMo 910 steel in all X, Y, and Z directions at 10 mm from the weld surface. The center of the processed stud displayed compressive stress followed by a tensile stress peak around the weld line and the gradual reduction in RS towards the BM. In the X direction, a 2D map exposed compressive RS at the mixed zone changing to tensile around the weld line, indicating a conical shape. As mentioned by the authors, the defects and cracks around were related to the tensile stress peaks in the weld line at the stud bottom and the flash. In another work developed by Hattingh et al. [24] with multiple FHPP, six overlapped studs presented different profiles. A neutron diffraction analysis performed on 13CrMo44 steel showed that the behavior differed according to each stud evaluated. In the case of the last overlapped stud, the horizontal profile showed a tensile strain peak outside the weld interface. From that point towards the BM, the values decreased until reaching the compressive field. Different depths measured from the center of the joint demonstrated a tensile strain field increasing toward the bottom of the stud, and the maximum tensile stress was detected outside of the joint, below the stud. In addition, the center stud, which had part of the weld zone replaced by a subsequent stud, developed higher strain values than the precedent stud. The authors related this behavior to the

geometric constraints generated during the welding of the successive studs. Other friction welding methods have also shown a similar tensile nature in the weld seam. According to the overview written by Misha et al. [3], friction stir welding applied to aluminum alloys (2000, 5000, 6000, and 7000 series) in butt welding configurations generated transversal and longitudinal tensile RS in the welding centerline. Moraes et al. [25] also found the same pattern in girth friction welding with tensile values lower than those of gas tungsten arc welding.

Post-weld heat treatment (PWHT) is a common industrial practice for restoring material properties, decreasing RS and hardness, and enhancing metallurgical and mechanical joint qualities. The efficiency of the stress relief depends on the chemical composition, temperatures involved, soaking time, and cooling rate applied [26]. James et al. [19] evaluated the effect of localized PWHT on the RS in a steam steel pipe repaired with a stud of BS EN 10216 Grade 10CrMo9-10. Neutron diffraction measurements indicated that the process developed compressive stresses ranging from 380 to 450 MPa in the hoop direction. The PWHT relieved the compressive stress setting between 275 and 380 MPa, representing 16% of the hoop maximum values. Amavisca et al. [18] used X-ray diffraction to analyze AISI H13 steel FHPP welds with PWHT. The authors measured a compressive field in the hole/stud interface with tensile peaks near the heat-affected zone (HAZ) of the BM. In addition, the profiles indicated a tensile RS in the middle of the stud with maximum values of about 100 MPa.

The abovementioned investigations highlight the effect of FHPP on residual stress. However, each material and welding procedure reflects different scenarios and outcomes. In this context, the importance of the assessment of residual stress applied to mooring chain steel by FHPP is crucial for determining structural integrity and defining the potential usage of FHPP as a repair process. In this sense, the present work aims to evaluate FHPP applied to grade R4 offshore mooring chain steel as a repair technique and the subsequent application of PWHT to restore the steel properties.

2. Materials and Methods

Samples with 28.6 mm diameter studs and $100 \times 50 \times 30 \text{ mm}^3$ plates were extracted from R4 grade offshore mooring steel bars in the heat-treated condition [2]; the chemical composition and mechanical properties of the mooring chain steel are presented in Table 1. A conical diameter reduction with a semi-spherical geometry was machined in the tip studs, and a blind hole was opened in the plates, as shown in Figure 2. The parameters applied to perform FHPP were 1500 rpm rotation speed, 45 kN axial force, and 7 mm burn-off, without gas protection, and an open-air environment in the friction welding machine MPF-1000 [27]. After the FHPP procedures, the PWHT parameters applied were 1, 2, and 4 h at 590 °C with subsequent air cooling.

Table 1. Chemical composition and properties of mooring chain steel (wt.%).

Chemical Composition (wt.%)										
C	Si	Mn	P	S	Cr	Mo	Ni	Al	Cu	Ti
0.214	0.250	0.980	0.005	0.008	1.060	0.252	0.533	0.012	0.151	0.002
Mechanical properties of API Specification 2F Grade R4 [2]										
Yield Strength Min. (N/mm ²)			Ultimate Tensile Strength Min. (N/mm ²)				Elongation Min. (%)			
580			860				12			

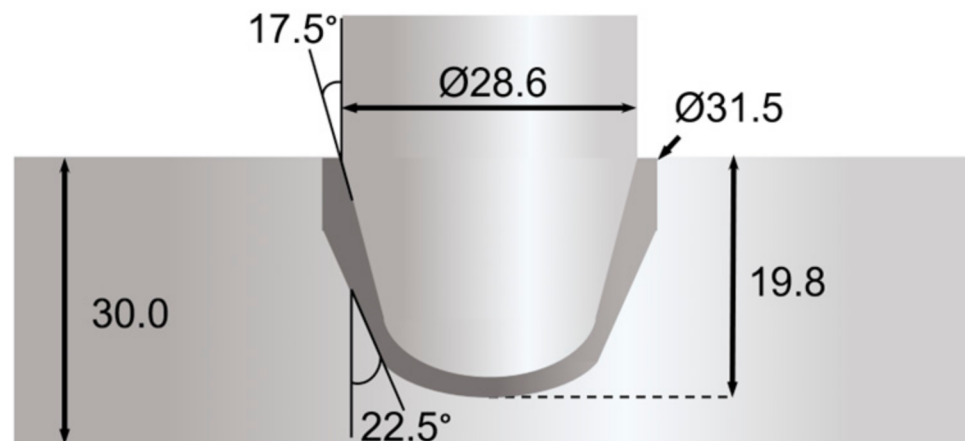


Figure 2. Geometry and dimensions (mm) of stud and BM.

Metallographic standards of grinding, polishing, and, finally, 5% Nital solution etching were developed in a cross-sectioned part of each FHPP sample. In addition, horizontal microhardness profiles of 300 gF every 2 mm and 0.3 mm from point to point were carried out to generate hardness mappings.

RS evaluation was performed using neutron diffraction measurements on beamline E3 of the BER II reactor at the Helmholtz-Zentrum Berlin (Berlin, Germany). At the primary beam path, a segmented elastically bent silicon monochromator was installed to give a high neutron flux. The diffracted beam was recorded with a ^3He position-sensitive detector of $300 \times 300 \text{ mm}^2$ size and 256×256 channels. Finally, a goniometer with an automatic XYZ-translation table was used. The distance between the diffractometer center and the detector was 1.3 m, with more details described by Poeste et al. [28].

In the incident beam, a mask with a cross-section of $3 \times 3 \text{ mm}^2$ was used. The aperture at the secondary side was 2 mm in width without height limitation. As the neutron beam had low divergence, the mask at the primary side and the aperture in the diffracted beam allowed a diffracting volume to be selected quite precisely. The scattering vector was perpendicular to the measured $\{hkl\}$ planes. Exclusively, the $\{211\}$ diffraction line of (α -Fe) was selected for the measurements. The wavelength for the experiments was 0.1486 nm, and the diffraction line position was around 78.8 degrees in 2θ . Volume elements in the diffractometer plane had a rhombohedral shape. The coordinate system of the measurements was placed at the central plane and in the centerline of the sample. Accordingly, the volume elements were placed at positions 3 mm to 88 mm, with 3 mm steps, where 34 different positions through the cross-sectioned samples determined the number of RS measurements. In addition, gauge volumes at 3 mm positions were partially immersed in the material. Deviations of line positions, called the surface effect, were expected with the use of plane apertures [28,29]. However, the setup of the instrument minimized these effects [30,31]. In addition, 2-dimensional data of the image plate detector were integrated, and the obtained diffraction lines were fitted by a Gaussian after background subtraction. Strains were calculated from positions of diffraction lines corresponding to the $\{hkl\}$ plane of the measured phase giving lattice spacing $d\{hkl\}$ through Bragg's law, and the stress-free lattice spacing d_0 . RSs in the considered directions were calculated by force equilibrium equations, for which more details are presented in [28]. As the incident neutron gauge volume was $3 \times 3 \times 3 \text{ mm}^3$, the irradiated areas touched each other, with the line mapping placed 25 mm from the bottom. Figure 3A displays the RS measurement position in red, and Figure 3B,C show the experimental setup.

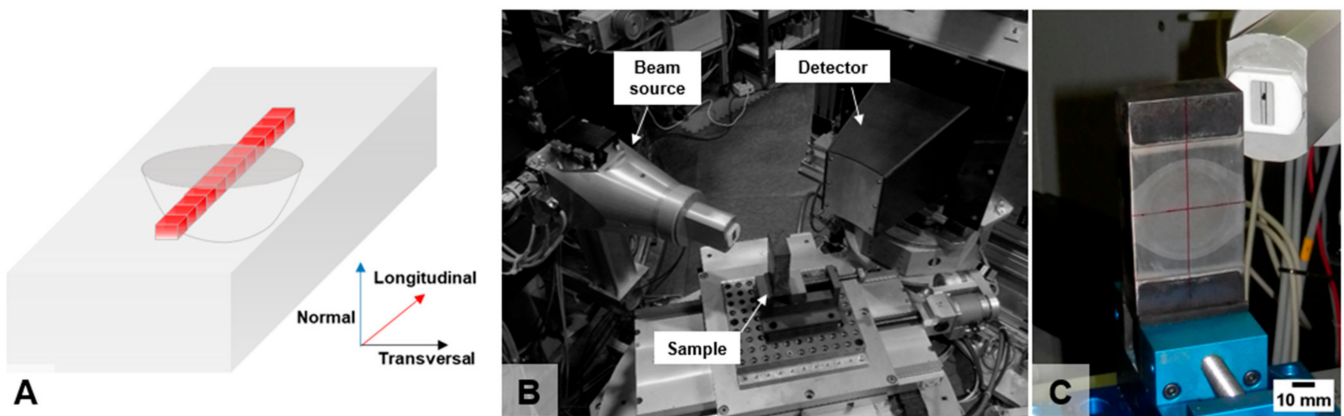


Figure 3. Schematic illustration of the RS gauge volumes (A), the experimental setup (B), and the as-repaired sample (C).

3. Results and Discussion

3.1. Joint Analyses

As an FHPP characteristic, the weldments displayed the weld line (WL) and both the thermo-mechanically affected zone (TMAZ) and heat-affected zone (HAZ) in the stud and the BM, as demonstrated in Figure 4. Initially, the rotational friction contact between the stud tip and the bottom cavity produces the heat input. The temperature generated reduces the stud and BM strength, allowing the stirring of the materials. The friction forces and the shear deformation with the successive adiabatic transformations increase the temperature, generating the TMAZs and filling the cavity. The extra material processed is extruded outside of the cavity, creating flashes with volumes related to the burn-off. The heat input also spreads to the parent materials, and the thermal cooling rates generate the HAZ [14]. The WL is a narrow layer between the stud and the BM formed through the extrusion of the materials extruded, as shown by Landell et al. [4].

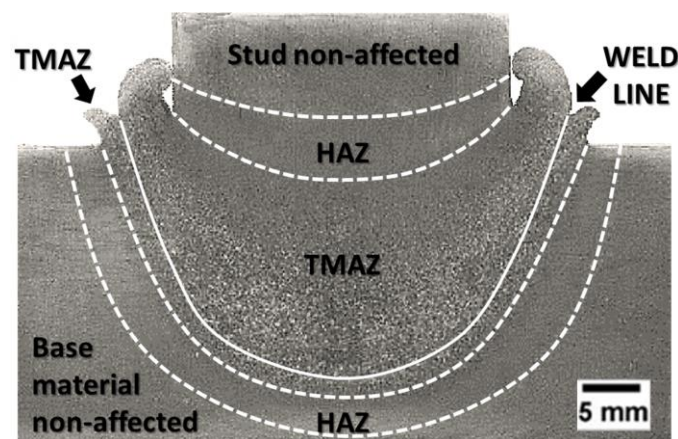


Figure 4. Macrograph of the joint showing the different zones generated by the FHPP.

Figure 5 exhibits microhardness mappings of different conditions. The hardness variations revealed the process effect, where the stud shape and zones are aligned with the macrographic analysis (lines of Figure 4). The HAZ from the BM displayed a microstructural and hardness variation due to the thermal gradient involved. This zone exhibited a gradual measurement variance, from 278 HV_{0.3} (near the BM) to a peak of 569 HV_{0.3} (closer to the TMAZ). This difference is a result of the thermal gradient subject during the process. Interestingly, the values detected in the HAZ were inferior to those of the BM (average of 346.2 HV_{0.3} and maximum of 368 HV_{0.3}), indicating a softening effect related to the heat flow with temperatures below the AC1. In contrast, the higher temperatures near TMAZ

exceeded the AC1, enhancing the hardness due to the re-austenitization (complete and partial) and the subsequent high cooling rates. This behavior was also observed by the authors of [32].

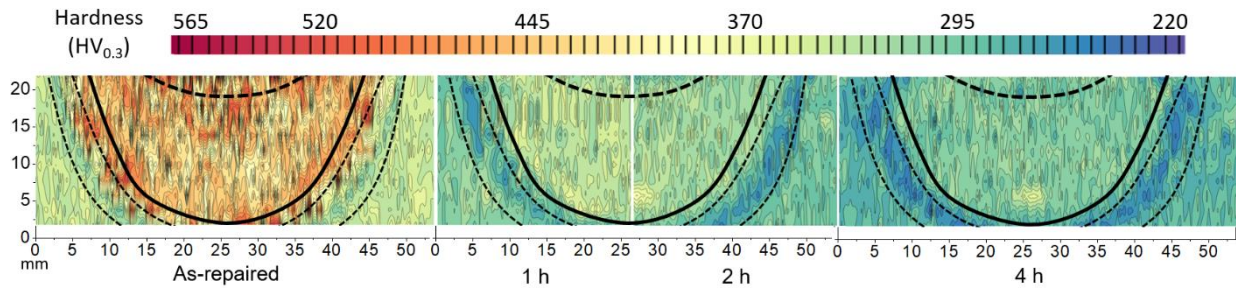


Figure 5. Hardness mapping of as-repaired condition and with 1, 2, and 4 h of PWHT.

Differently from the HAZ, in which the microstructural modifications were mostly a consequence of the thermal cycle, the TMAZ presented microstructural transformations caused by the simultaneous effects of the stud metal shearing, the axial force, and the temperature variation. Both TMAZs of the BM and the stud showed levels between 320 and 569 HV_{0.3} with a smooth hardness reduction in the processed center, due to the cooling rate variations. Between these zones, the flow of the stud and BM generated the WL.

Predictably, the 1 h PWHT application showed a significant influence on the hardness. With the increase in the treatment time, the hardness variation effect was minor compared with the 1 h treatment. Furthermore, the 4 h condition reduced the hardness below the parent material levels, displaying a low difference between the processed region and the BM.

Based on the hardness mapping measurements, a detailed examination of the TMAZ and HAZ indicated a descending profile with the PWHT. The chart in Figure 6A shows an expressive hardness decrease, especially in the maximum values, ranging from 551 HV_{0.3} in the as-repaired sample to 362 HV_{0.3} after 4 h PWHT in the TMAZ. As noted, the average was reduced to below the maximum BM hardness (368 HV_{0.3}) after 1 h. The BM HAZ displayed similar behavior in all tempering conditions, generating hardness below the BM values, as shown in Figure 6B. In this case, the increment in the heat treatment time did not exhibit a prominent variation.

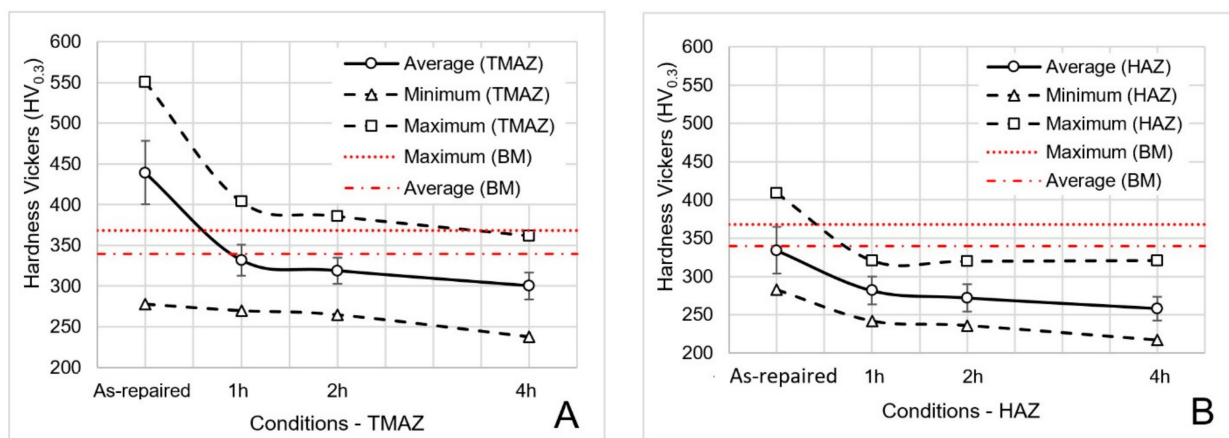


Figure 6. Hardness of the as-repaired condition and PWHT conditions in the TMAZ (A) and HAZ (B), where the red dashed line corresponds to the maximum BM hardness.

The PWHT effect was observed in the crystallographic modifications. As demonstrated in Figure 7A, the HAZ presented a tempered martensitic phase. This microstructure

is the result of the temperature variation that the previous martensitic phase was subjected to since it is more strongly susceptible to tempering temperature than other microstructures [33]. Consequently, a decrease in the hardness measurements was detected.

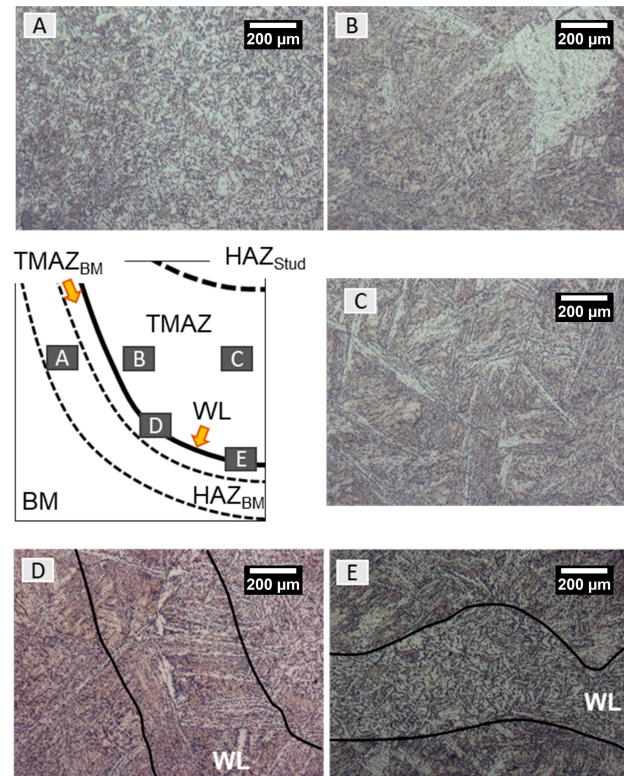


Figure 7. Microstructure analysis of the PWHT joint on (A) BM TMAZ, (B) lateral of the stud TMAZ, (C) center of the stud TMAZ, (D) WL, and (E) bottom WL.

Nevertheless, in the TMAZ, the complex mechanism of temperature gradients and high plastic deformation level modified the parent material to a stirring refined structure. In this case, 4 h tempering produced a microstructure composed of lower and upper bainite, bainitic ferrite with non-aligned carbide, and tempered martensite. Therefore, the lower bainite and the tempered martensite were predominantly in the surrounding area, and the upper and lower bainite were in the TMAZ center, as shown in Figure 7B,C, respectively. This slight microstructure variation is a consequence of the difference in the thermal gradients developed during the process. Whereas the temperature in the center declines with lower rates due to the higher heat accumulation, the surrounding area exhibits faster thermal cooling rates. In the WL, as demonstrated in Figure 7D, the microstructure had the same TMAZ feature. However, the intensive friction and plastic deformation promoted a mainly refined tempered martensite in the bottom of the stud, as shown in Figure 7E.

3.2. Residual Stress Evaluation

Figure 8 presents the full width at half maximum (FWHM) of the neutron diffraction data for as-repaired conditions in the three directions and a hardness profile at 4 mm from the surface. As used by Yi et al. [34] and Amavisca et al. [18], the FWHM results were displayed with a relevant hardness curve to provide a better comprehension. Furthermore, as commented by Chen et al. [35], hardness is a result of elasticity, plasticity, work hardening capability, mechanical strength, and toughness data, where angular diffraction is indicative of strain hardening, micro-strain, dislocation density, and grain refinement.

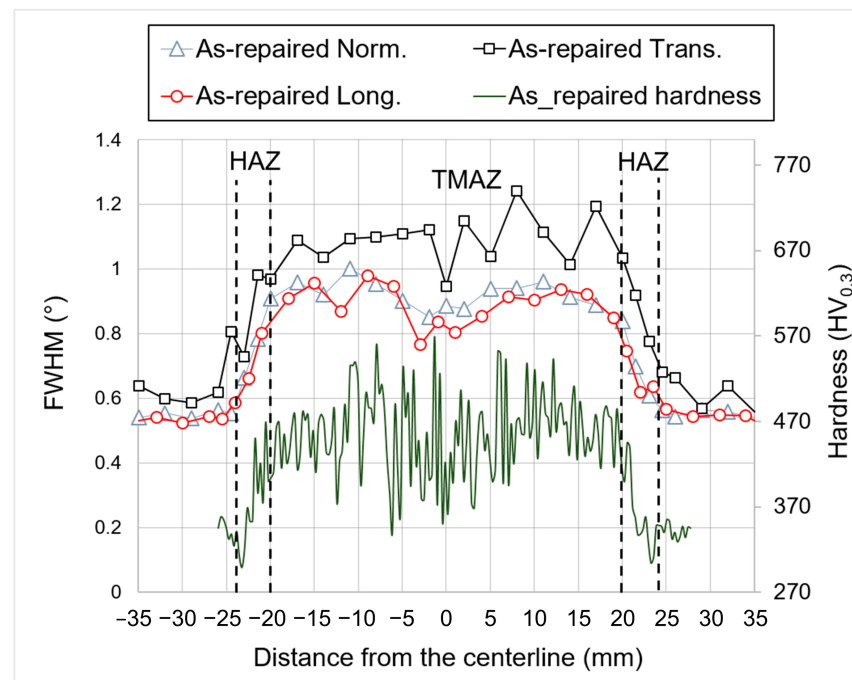


Figure 8. Longitudinal, transversal, and normal FWHM and as-repaired hardness at 4 mm from the top.

As observed in the as-repaired profile, FHPP affected the TMAZ in the range of ± 20 mm, in which the material underwent the highest plastic deformation levels. The effects of the microstructure variation, dislocation density, and hardness decrease promoted an angular reduction in the HAZ from ± 20 mm to about 24 mm. However, even with the hardness decreasing to about 300 HV_{0.3} (below the parent material), the angles were superior to the BM, differently from those observed in [34]. This effect is probably due to the micro-strain and dislocation density involved in this technique. In the BM, the as-repaired profile displayed a scatter of about 0.55° in the normal and the longitudinal directions and a slight increase of about 0.6° in the transversal direction. As shown in Figure 9, the 4 h PWHT profile assumed angles of 0.45° and 0.55° in all directions across the material repaired. In both situations, for the as-repaired and 4 h PWHT, the scatter was superior to 0.1° found by Hirsh et al. [36] in normalized steels, demonstrating different FWHM behaviors affected by the processes.

FHPP affected the parent material RS in the longitudinal, transversal, and normal directions, with distinguished behaviors, as demonstrated in Figure 10. The normal direction RS showed a scatter profile with tensile values between 16 and 118 MPa in all zones affected (in the range of ± 26 mm). The transversal RS profile presented an “M” format with a gradual variation from the BM to reach tensile peaks of about 310 MPa placed at ± 23 mm, both coincident with the softness zone of the BM HAZ. However, the tensile nature sharply changed to compressive behavior in the stud TMAZ (in the range of ± 20 mm) with a maximum of 126 MPa. Differently, the longitudinal direction presented an inverted “M” format, gradually decreasing from the BM to about -150 MPa at positions of ± 24 mm (softness zone) and adopting a tensile feature in the TMAZ (peak of 166 MPa). In fact, the measurements showed transversal tensile and longitudinal compressive peaks in the softness zone. Other authors revealed this same pattern, even with other materials or processes. Amavisca et al. [18] noticed it when applying the counter method and the X-ray method in FHPP. Roy et al. [37] and Yiet al. [34] found it in all directions in the clad process. Interestingly, in investigations conducted with preheat applied to ultra-high-strength steel, and Sun and Dilger [38] observed an RS profile similar to that presented in this work. However, the TIG process generated high levels of tensile RS nature in the fusion zone. As

also demonstrated by Akrivos et al. [39], Inconel plates filled with alloy 82 filler resulted in tensile RS in the transversal and longitudinal directions and compressive behavior at the beginning and at the end HAZ of the weld bead in the transversal direction.

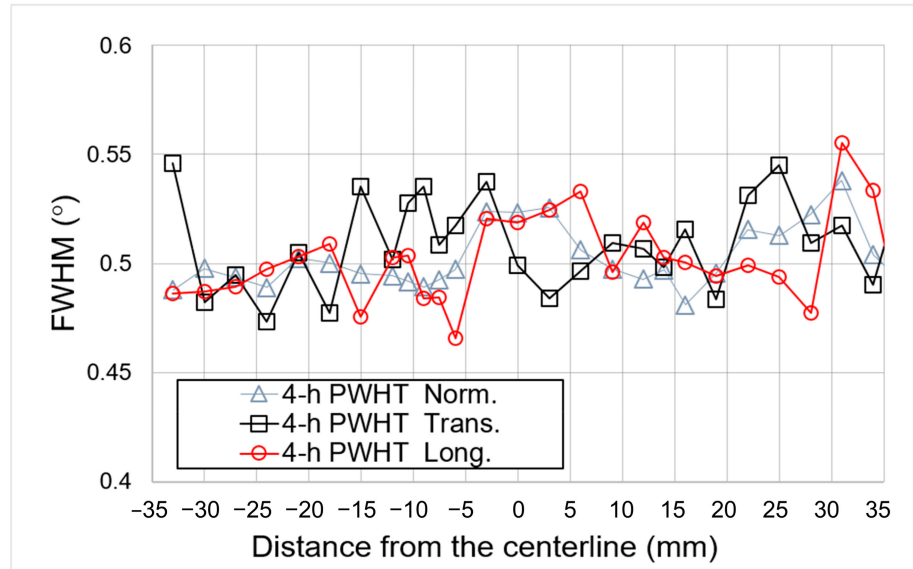


Figure 9. Longitudinal, transversal, and normal FWHM for the 4 h PWHT.

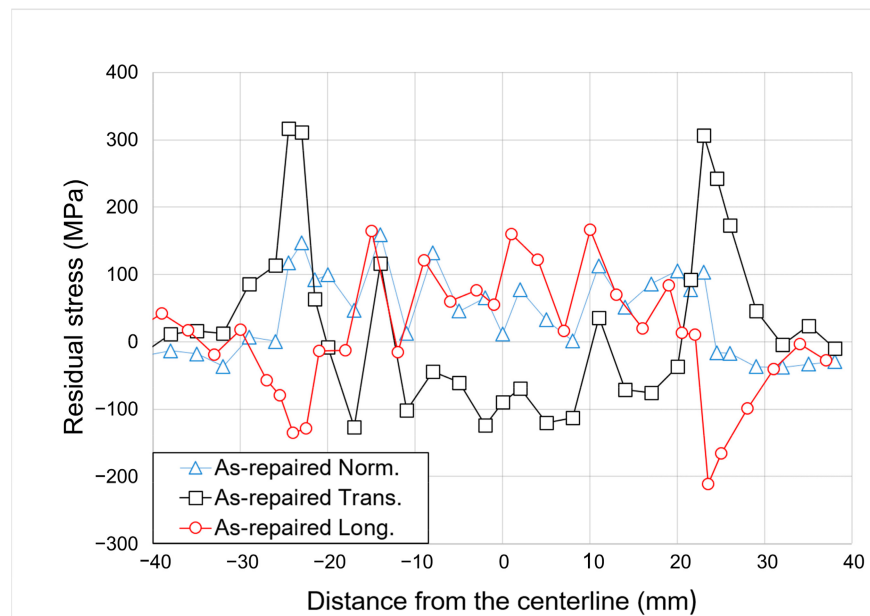


Figure 10. Longitudinal, transversal, and normal RS plotted against the Z-axis position of the as-repaired sample.

As expected, the PWHT significantly decreased the longitudinal, transversal, and normal RS, generating similar and homogeneous profiles, as presented in Figure 11. During the 4 h tempering process, the RS was gradually relieved due to the crystallographic modification and dislocation density reduction. This performance was similar to the behavior noted in the hardness measurements.

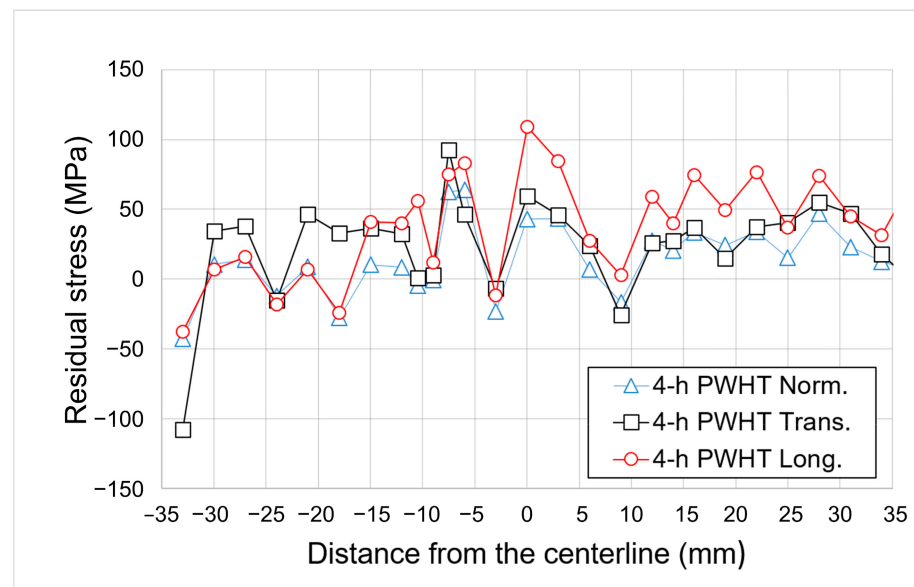


Figure 11. Longitudinal, transversal, and normal RS plotted against the z-axis position of the PWHT sample.

In general, the outcomes of this study indicate that the use of FHPP technology is a potential method for repairing offshore components. In the case of the as-repaired condition, the processed zone resulted in a microstructural formation and a significant rise in the hardness, both beneficial to the wear resistance. Nevertheless, the TMAZ RS analysis showed compressive stress varying from 0 to 126 MPa in the transversal direction and a tensile distribution from 0 to 166 MPa in the normal and longitudinal directions, where the maximums corresponded to 29% yield strength and 19% ultimate tensile strength of the parent material. The BM HAZ exhibited the highest tensile peaks in the transversal direction, reaching values of 307 and 317 MPa (55% yield strength and 37% ultimate tensile strength). However, the method produced compressive stress in the longitudinal direction, with peaks of -135 and -212 MPa located in the same zone of the low levels of hardness (300 HV_{0.3}), known as the softening zone.

The use of PWHT to restore steel properties can play an expressive role as a viable alternative to mitigate the hardness and the RS. The heat treatment of 4 h promoted a hardness reduction with values below those of the BM. With regard to the RS, the maximum tensile stress field reached 109 MPa, equivalent to 18% of the yield strength and 12% of the ultimate tensile strength. Following PWHT conditions, the TMAZ hardness average was lowered below the BM values in just one hour. This indicates that this heat condition could be applied to achieve the parent material status.

In addition, the present study also reveals another advantage of this repair technique. The use of studs with the same parent material restores the homogeneity of the mended component in terms of chemical, physical, and mechanical properties. However, further investigations shall be carried out to evaluate other aspects, such as fatigue properties.

4. Conclusions

The investigation of FHPP as a repair technique was carried out with the grade R4 offshore mooring chain steel. The findings of the current study can be summarized as follows:

- The residual stress analysis exhibited distinguished behaviors in all directions with a typical “M” shape behavior with tensile peaks in the HAZ and compressive peaks in the TMAZ in the transversal direction. However, an inverted “M” format was observed in the longitudinal direction, and a scatter tensile profile was observed in

the normal direction. The PWHT restored the RS properties, generating similar and homogeneous profiles in all directions.

- The microhardness analysis of the as-repaired condition revealed a significant increase in the TMAZ and a reduction in the HAZ softening zone.
- With the 4 h PWHT condition, the maximum hardness values were reduced below those of the parent material. The microstructure evaluation presented a tempered martensitic phase in the HAZ and a mixture of lower and upper bainite, bainitic ferrite with non-aligned carbide, and tempered martensite in the TMAZ.

Author Contributions: Conceptualization, M.T.P.P., R.R.M. and A.R.; methodology, R.E.d.S. and R.M.N.; investigation, R.E.d.S., M.C. and R.M.N.; resources, M.T.P.P. and R.R.M.; writing—original draft preparation, R.E.d.S., M.C. and R.M.N.; writing—review and editing, R.E.d.S., M.C., R.M.N. and M.T.P.P.; project administration, M.T.P.P., R.R.M. and A.R. All authors have read and agreed to the published version of the manuscript.

Funding: This research received no external funding.

Data Availability Statement: Data will be made available on request.

Acknowledgments: The authors would like to thank Gerdau S.A. for material supply and the financial support from Petrobras and ANP (Brazilian Agency for Petroleum and Energy). The authors gratefully acknowledge the award of beam-time on the Helmholtz-Zentrum Berlin für Materialien und Energie GmbH and assistance from the beamline scientist, Robert Wimpory. In addition, the authors express their gratitude to Telmo R. Strohaecker, whose presence and wisdom will be profoundly missed.

Conflicts of Interest: The authors declare no conflict of interest.

References

1. Mandal, N.R. *Ship Construction and Welding*; Springer: Berlin/Heidelberg, Germany, 2017; Volume 2; ISBN 978-981-10-2953-0.
2. IACS. *2008 Requirements Concerning Materials and Welding*; International Association of Classification Societies: London, UK, 2016.
3. Mishra, R.; Kumar, N. *Friction Stir Welding and Processing*; Springer International Publishing: Cham, Switzerland, 2014; ISBN 9783319070421.
4. Landell, R.; Kanan, L.F.; Buzzatti, D.; Vicharapu, B.; De, A.; Clarke, T. Material Flow during Friction Hydro-Pillar Processing. *Sci. Technol. Weld. Join.* **2019**, *25*, 228–234. [[CrossRef](#)]
5. Bevilacqua, M.; Ciarapica, F.E.; D’Orazio, A.; Forcellese, A.; Simoncini, M. Sustainability Analysis of Friction Stir Welding of AA5754 Sheets. *Procedia CIRP* **2017**, *62*, 529–534. [[CrossRef](#)]
6. Elyasi, M.; Taherian, J.; Hosseinzadeh, M.; Kubit, A.; Derazkola, H.A. The Effect of Pin Thread on Material Flow and Mechanical Properties in Friction Stir Welding of AA6068 and Pure Copper. *Heliyon* **2023**, *9*, e14752. [[CrossRef](#)] [[PubMed](#)]
7. Joshani, E.; Beidokhti, B.; Davodi, A.; Amelzadeh, M. Evaluation of Dissimilar 7075 Aluminum/AISI 304 Stainless Steel Joints Using Friction Stir Welding. *J. Alloys Metall. Syst.* **2023**, *3*, 100017. [[CrossRef](#)]
8. Buzzatti, D.T.; Buzzatti, J.T.; dos Santos, R.E.; Mattei, F.; Chludzinski, M.; Strohaecker, T.R. Friction Hydro Pillar Processing: Characteristics and Applications. *Soldag. Inspeção* **2015**, *20*, 287–299. [[CrossRef](#)]
9. Vyas, H.D.; Mehta, K.P.; Badheka, V.; Doshi, B. Processing and Evaluation of Dissimilar Al-SS Friction Welding of Pipe Configuration: Nondestructive Inspection, Properties, and Microstructure. *Meas. J. Int. Meas. Confed.* **2021**, *167*, 108305. [[CrossRef](#)]
10. Joshi, G.R.; Badheka, V.J.; Darji, R.S.; Oza, A.D.; Pathak, V.J.; Burduhos-Nergis, D.D.; Burduhos-Nergis, D.P.; Narwade, G.; Thirunavukarasu, G. The Joining of Copper to Stainless Steel by Solid-State Welding Processes: A Review. *Materials* **2022**, *15*, 7234. [[CrossRef](#)]
11. Ahmad Mir, F.; Zaman Khan, N.; Noor Siddiquee, A.; Parvez, S. Friction Based Solid State Welding—A Review. *Mater. Today Proc.* **2022**, *62*, 55–62. [[CrossRef](#)]
12. Meyer, A. *Friction Hydro Pillar Processing*; Technischen Universität Braunschweig: Braunschweig, Germany, 2002.
13. Iracheta, O.; Bennett, C.J.; Sun, W. A Sensitivity Study of Parameters Affecting Residual Stress Predictions in Finite Element Modelling of the Inertia Friction Welding Process. *Int. J. Solids Struct.* **2015**, *71*, 180–193. [[CrossRef](#)]
14. Wang, Y.; Sebeck, K.; Tess, M.; Gingrich, E.; Feng, Z.; Haynes, J.A.; Lance, M.J.; Muralidharan, G.; Marchel, R.; Kirste, T.; et al. Interfacial Microstructure and Mechanical Properties of Rotary Inertia Friction Welded Dissimilar 422 Martensitic Stainless Steel to 4140 Low Alloy Steel Joints. *Mater. Sci. Eng. A* **2023**, *885*, 145607. [[CrossRef](#)]
15. Khalfallah, F.; Boumerzoug, Z.; Rajakumar, S.; Raouache, E. Optimization by RSM on Rotary Friction Welding of AA1100 Aluminum Alloy and Mild Steel. *Int. Rev. Appl. Sci. Eng.* **2020**, *11*, 34–42. [[CrossRef](#)]
16. Nicholas, E.D.; Jones, S.B.; Lilly, R.H.; Dawes, C.J.; Dolby, R.E. Friction Forming. European Patent Specification 0602072B1, 1992.

17. Pinheiro, G.A. *Local Reinforcement of Magnesium Components by Friction Processing: Determination of Bonding Mechanisms and Assessment of Joint Properties*; Technischen Universität Hamburg-Harburg: Harburg, Germany, 2008.
18. Amavisca, C.V.; Cordenonsi da Fonseca, G.; Diehl, I.L.; Buzzatti, D.T.; Rosauro Clarke, T.G. Investigation of the Residual Stress Distribution in Repairs in H13 Steel by Friction Hydro Pillar Processing. *Sci. Technol. Weld. Join.* **2020**, *25*, 503–510. [[CrossRef](#)]
19. James, M.N.; Hattingh, D.G.; Asquith, D.; Newby, M.; Doubell, P. Residual Stresses in Condition Monitoring and Repair of Thermal Power Generation Components. *Theor. Appl. Fract. Mech.* **2017**, *92*, 289–297. [[CrossRef](#)]
20. Toribio, J.; Lorenzo, M.; Vergara, D.; Kharin, V. Effects of Manufacturing-Induced Residual Stresses and Strains on Hydrogen Embrittlement of Cold Drawn Steels. *Procedia Eng.* **2011**, *10*, 3540–3545. [[CrossRef](#)]
21. Withers, P.J.; Bhadeshia, H.K.D.H. Residual Stress Part 1—Measurement Techniques. *Mater. Sci. Technol.* **2001**, *17*, 355–365. [[CrossRef](#)]
22. Paes, M.T.P. *Processamento Termomecânico de Pinos de Aço no Interior de Cavidades de Aço C-Mn Através de Soldagem Por Atrito Rotacional*; Universidade Federal do Rio de Janeiro: Rio de Janeiro, Brazil, 2013.
23. Hattingh, D.G.; Bulbring, D.L.H.; Els-Botes, A.; James, M.N. Process Parameter Influence on Performance of Friction Taper Stud Welds in AISI 4140 Steel. *Mater. Des.* **2011**, *32*, 3421–3430. [[CrossRef](#)]
24. Hattingh, D.G.; Steuwer, A.; James, M.N.; Wedderburn, I.N. Residual Stresses in Overlapping Friction Taper Stud Welds. *Mater. Sci. Forum* **2010**, *652*, 111–115. [[CrossRef](#)]
25. De Moraes, C.A.P.; Chludzinski, M.; Nunes, R.M.; Lemos, G.V.B.; Reguly, A. Residual Stress Evaluation in API 5L X65 Girth Welded Pipes Joined by Friction Welding and Gas Tungsten Arc Welding. *J. Mater. Res. Technol.* **2019**, *8*, 988–995. [[CrossRef](#)]
26. Lancaster, J.F. *Handbook of Structural Welding*; Woofhead Publishing Ltd.: Cambridge, UK, 1997.
27. Buzzatti, D.T.; Chludzinski, M.; Dos Santos, R.E.; Buzzatti, J.T.; Lemos, G.V.B.; Mattei, F.; Marinho, R.R.; Paes, M.T.P.; Reguly, A. Toughness Properties of a Friction Hydro Pillar Processed Offshore Mooring Chain Steel. *J. Mater. Res. Technol.* **2019**, *8*, 2625–2637. [[CrossRef](#)]
28. Poeste, T.; Wimpory, R.C.; Schneider, R. The New and Upgraded Neutron Instruments for Material Science at HMI—Current Activities in Cooperation with Industry. *Mater. Sci. Forum* **2006**, *524–525*, 223–228. [[CrossRef](#)]
29. Gibmeier, J.; Kornmeier, J.; Hofmann, M. Neutron Diffraction Stress Analysis of near Surface Stress Gradients of Surface Treated Steel Samples. *Adv. X-ray Anal.* **2009**, *52*, 279–286.
30. Webster, G.A.; Wimpory, R.C. Development of Procedures for the Measurement of Residual Stress by Neutron Diffraction. *Appl. Phys. A Mater. Sci. Process.* **2002**, *74*, S1227–S1229. [[CrossRef](#)]
31. Wimpory, R.C.; Ohms, C.; Hofmann, M.; Schneider, R.; Youtsos, A.G. Statistical Analysis of Residual Stress Determinations Using Neutron Diffraction. *Int. J. Press. Vessel. Pip.* **2009**, *86*, 48–62. [[CrossRef](#)]
32. Hu, L.; Li, X.; Luo, W.; Li, S.; Deng, D. Residual Stress and Deformation in UHS Quenched Steel Butt-Welded Joint. *Int. J. Mech. Sci.* **2023**, *245*, 108099. [[CrossRef](#)]
33. Bhadeshia, H.K.D.H. *Bainite in Steels Theory and Practice*, 3rd ed.; CRC Press: London, UK, 2019; ISBN 9781909662742.
34. Yi, J.; Gharghoury, M.; Bocher, P.; Medraj, M. Distortion and Residual Stress Measurements of Induction Hardened AISI 4340 Discs. *Mater. Chem. Phys.* **2013**, *142*, 248–258. [[CrossRef](#)]
35. Chen, M.; Xing, S.; Liu, H.; Jiang, C.; Zhan, K.; Ji, V. Determination of Surface Mechanical Property and Residual Stress Stability for Shot-Peened SAF2507 Duplex Stainless Steel by in Situ X-Ray Diffraction Stress Analysis. *J. Mater. Res. Technol.* **2020**, *9*, 7644–7654. [[CrossRef](#)]
36. Hirsh, T.K.; Rocha, A.d.S.; Nunes, R.M. Characterization of Local Residual Stress Inhomogeneities in Combined Wire Drawing Processes of AISI 1045 Steel Bars. *Int. J. Adv. Manuf. Technol.* **2014**, *70*, 661–668. [[CrossRef](#)]
37. Roy, T.; Paradowska, A.; Abrahams, R.; Law, M.; Mutton, P.; Soodi, M.; Yan, W. Residual Stress in Laser Cladded Heavy-Haul Rails Investigated by Neutron Diffraction. *J. Mater. Process. Technol.* **2020**, *278*, 116511. [[CrossRef](#)]
38. Sun, J.; Dilger, K. Influence of Preheating on Residual Stresses in Ultra-High Strength Steel Welded Components. *J. Mater. Res. Technol.* **2023**, *25*, 3120–3136. [[CrossRef](#)]
39. Akrivos, V.; Muransky, O.; Depradeux, L.; Smith, M.C.; Vasileiou, A.; Deaconu, V.; Kapadia, P. On the Accurate Prediction of Residual Stress in a Three-Pass Slot Nickel-Base Repair Weld by Numerical Simulations. *J. Manuf. Mater. Process.* **2022**, *6*, 61. [[CrossRef](#)]

Disclaimer/Publisher’s Note: The statements, opinions and data contained in all publications are solely those of the individual author(s) and contributor(s) and not of MDPI and/or the editor(s). MDPI and/or the editor(s) disclaim responsibility for any injury to people or property resulting from any ideas, methods, instructions or products referred to in the content.